A Microthermal Sensor for Cryoablation Balloons

Harishankar Natesan
Department of Mechanical Engineering,
University of Minnesota,
Minneapolis, MN 55455

Limei Tian
Department of Biomedical Engineering,
Texas A&M University,
College Station, TX 77843

John A. Rogers
Department of Materials Science and Engineering,
Northwestern University,
Evanston, IL 60208

John Bischof
Department of Mechanical Engineering,
University of Minnesota,
Minneapolis, MN 55455

Treatment of atrial fibrillation by cryoablation of the pulmonary vein (PV) suffers from an inability to assess probe contact, tissue thickness, and freeze completion through the wall. Unfortunately, clinical imaging cannot be used for this purpose as these techniques have resolutions similar in scale (~1 to 2 mm) to PV thickness and therefore are unable to resolve changes within the PV during treatment. Here, a microthermal sensor based on the "3ω" technique which has been used for thin biological systems is proposed as a potential solution and tested for a cryoablation scenario. First, the sensor was modified from a linear format to a serpentine format for integration onto a flexible balloon. Next, using numerical analyses, the ability of the modified sensor on a flat substrate was studied to differentiate measurements in limiting cases of ice, water, and fat. These numerical results were then complemented by experimentation by micropatterning the serpentine sensor onto a flat substrate and onto a flexible balloon. In both formats (flat and balloon), the serpentine sensor was experimentally shown to: (1) identify tissue contact versus fluid, (2) distinguish tissue thickness in the 0.5 to 2 mm range, and (3) measure the initiation and completion of freezing as previously reported for a linear sensor. This study demonstrates proof of principle that a serpentine 3ω sensor on a balloon can monitor tissue contact, thickness, and phase change which is relevant to cryo and other focal thermal treatments of PV to treat atrial fibrillation. [DOI: 10.1115/1.4047134]

Keywords: thermal sensing, atrial fibrillation, biosensor, cryoballoon, precision treatment, thermal therapy, thermal property, 3ω method, cryoablation

Introduction

Thermal therapy is used to treat a variety of cardiovascular and cancer disease [1–3]. A major challenge with this therapy is delivering a precise and controlled thermal destruction to the target tissue while preventing damage to adjacent critical structures. Thermal therapy techniques such as radio frequency and microwave depend on the ability of the probe to electrically couple to the tissue, which allows the probe to be monitored by electrical impedance measurements at the probe surface to indicate if the tissue has become too dehydrated for efficient electrical conduction (i.e., Joule heating) and/or dielectric heating [4]. While this can be useful in terms of modifying the probe conditions, it does not directly relate to the amount of tissue treated. On the other hand, cryoablation, which destroys tissue by freezing, can use imaging modalities such as ultrasound [5–9], computed tomography [10–12], and magnetic resonance imaging [13–17] to visualize the entire cm scale frozen treatment zone. Unfortunately, this monitoring becomes ineffective when the characteristic size of the tissue approaches the limits of clinical imaging in thin tissues (mm thick). Thus, there is an unmet need to efficiently monitor balloon-based therapies in thin vascular structures such as the pulmonary vein (PV) for treatment of atrial fibrillation (AF), which affects millions of people every year. If left untreated, AF can contribute to the progression of further cardiovascular disease, stroke and even death. While some drugs can help control atrial fibrillation, they have side effects, and their efficacy is not uniform and often diminishes over time. Thus, the use of focal and especially thermal interventions to electrically isolate the PV thereby avoiding drugs is considered a milestone advancement in the treatment of AF [18,19]. Specifically, thermal and cryoablation for PV isolation have been used for more than 20 years and have become a standard of care for drug-refractory paroxysmal atrial fibrillation [18,20–26]. However, these treatments suffer from an inability to image or monitor the thermal therapy, leading to cases of over- and under-treatment. Indeed, over-treatment can lead to hemoptysis, esophageal freezing, or phrenic nerve palsy [24,27,28], and under-treatment requires repeat treatments [29,30]. Thus, as imaging cannot work on these thin mm-sized tissues, alternatives are urgently needed to improve the monitoring of balloon-based thermal and focal therapy.

Monitoring at the surface of the probes can be achieved in a rudimentary way with thermocouples [31] or more robustly using thermal conductivity changes with microsensors based on the 3ω technique [32,33,34] modified for thin biological systems [35]. Figure 1 (*a*, left) shows our original published embodiment of a 3ω sensor deposited on a flat substrate. This 3ω sensor can sense tissue or fluid contact, flow, mm-scale tissue thickness, and the initiation and completion of freezing, and it can be used to measure thermal conductivity (k) of thin (<2 mm) biological tissues [35,36]. It uses a sensor made up of a long, thin gold heater line (3 mm × 20 μm × 100 nm) deposited on a glass substrate. The biological tissue of interest is placed on top of the sensor such that it covers the heater line. An alternating current of frequency ω excites the heater line, producing temperature oscillations of frequency 2ω that propagate into the sample and the substrate over a thermal penetration depth, $\mathrm{PD} = (\alpha/2\omega)^{0.5}$, where α is thermal diffusivity (m^2/s) and ω is the frequency of the applied electric current (radians). The resulting third harmonic voltage across the heater line 3ω contains information about the temperature oscillations at the heater line. The temperature oscillations at the heater line can be used to calculate thermal conductivity of the sample with knowledge of the thermal and electrical properties of the sensor [32].

However, as cryoablation and other focal therapies in the PV are generally performed with balloons, there is a further need to integrate 3ω sensors onto balloons to perform the same sensing and monitoring functions. Recent advancements in flexible electronics now allow multiple types of sensors including 3ω sensors to be attached to flexible, stretchable substrates [37–42]. The current collaborative effort now integrates 3ω sensors directly onto a balloon for monitoring thermal therapy. Example designs that

Manuscript received January 27, 2019; final manuscript received April 20, 2020; published online September 8, 2020. Editor: Beth A. Winkelstein.

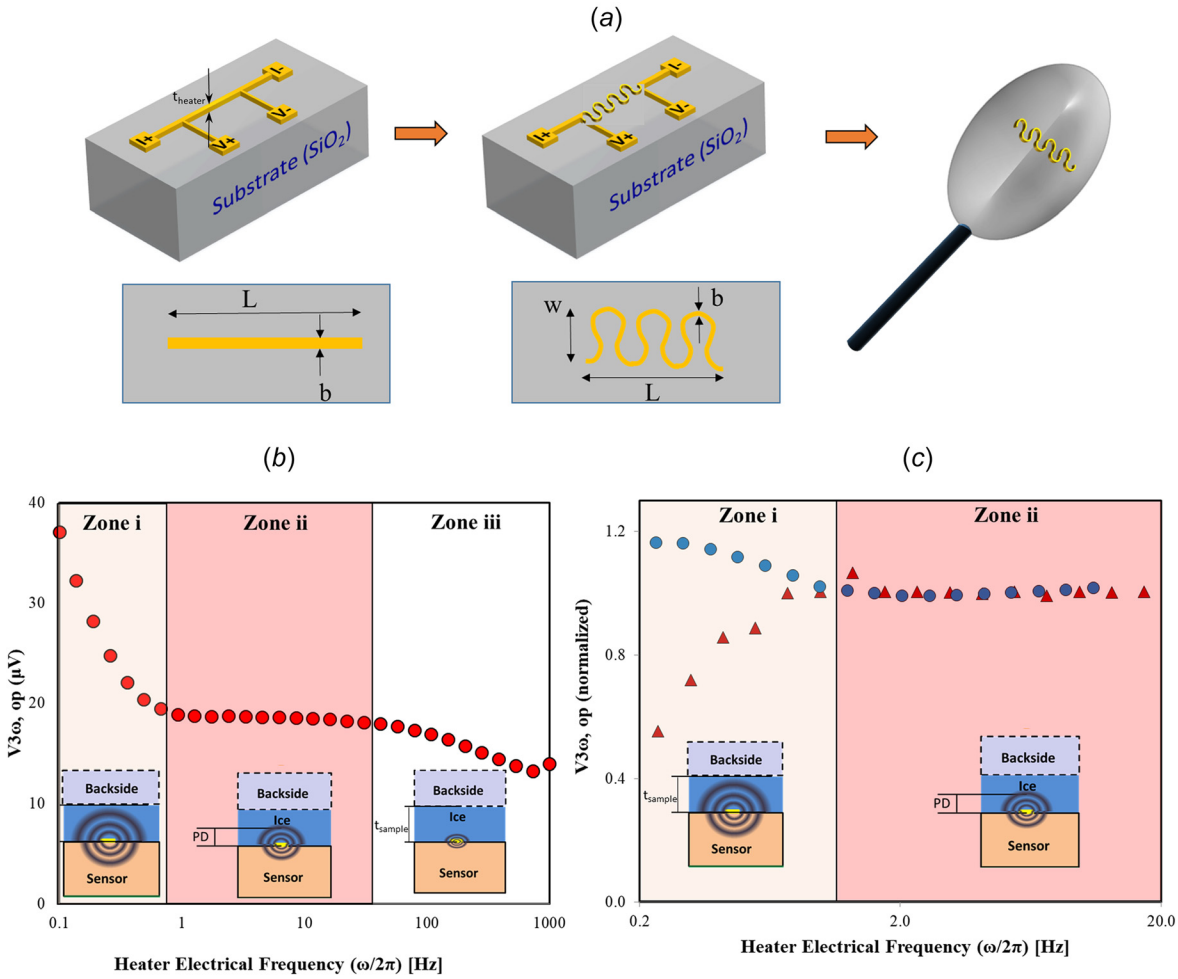

Fig. 1 Development of microthermal 3ω sensors for monitoring balloon cryoablation in PV: (*a*) Development of a microthermal sensor starting from a linear sensor ($L = 2$ mm, $b = 20$ μm) on a flat substrate, to a serpentine sensor ($L = 0.5$ mm, $b = 5$ μm, $w = 180$ μm). Finally, the serpentine sensor was integrated onto a balloon for focal therapy applications. (*b*) Historical data for a linear sensor show $V_{3\omega,op}$ as a function of heater electrical frequency ($\omega/(2\pi)$) where the sample is ice and backside boundary is air. Zone i refers to the frequency range where PD $\sim t_{sample}$. Zone iii refers to the range where PD $\sim t_{heater}$; zone ii refers to the range where $V_{3\omega,op}$ is neither affected by the heater line (PD $\gg t_{heater}$) nor the backside boundary condition ($\sim$100 nm) (PD $\ll t_{sample}$). Inset schematic shows the comparison between PD and sample thickness, t_{sample}, for zones i, ii, and iii. (*c*) Historical data for a linear sensor show $V_{3\omega,op}$ (*y*-axis) at low frequencies in zone i depends on a backside boundary for fixed sample thickness ($t_{sample} \approx 0.5$ mm). Blue circle data represent the case where a backside of the sample is low *k* plastic (quasi-adiabatic), and red triangle data represent the case where the backside is high *k* copper at fixed temperature (quasi-isothermal). Inset schematic shows the comparison between PD and t_{sample} for zones i and ii. Figs. 1(*b*) and 1(*c*) is reused without modification from Ref. [36]. The link to license: https://creativecommons.org/licenses/by/4.0/legalcode.

integrate electronic sensors onto balloons [38–40] and human skin [41] have already been published. Further, the theoretical and experimental study of the ability of 3ω to track phase front have already been studied. In this work, we modify the linear 3ω sensor design from a thin straight line to a serpentine shape to enable its integration onto a flexible, stretchable balloon as shown in Fig. 4.1 (a). The serpentine shape minimizes local strains during inflation and deflation of the balloon as previously reported for other sensors [37–41]. Hence, the modified sensor is first numerically analyzed using finite element modeling (using COMSOL) on a flat substrate to determine the ability to differentiate between ice, water and fat. Further, the sensor was investigated for its ability to sense thickness and phase change for ice and water, respectively. Next, these results were confirmed experimentally to sense tissue contact, thickness, and phase change. Finally, we microfabricated the sensor onto a flexible, stretchable balloon using transfer printing techniques (Fig. 4.1 (a)) [40]. The sensor on a balloon was then tested to sense contact, thickness, and phase change for possible cryotherapy (or other thermal therapy) application. A nomenclature table has been added in the SI to assist the readers in better understanding the principle and operation of the sensor as described in the Methods section.

Methods

Numerical Characterization of the Serpentine 3ω Sensor on a Flat Substrate

Principle of 3ω Sensor. The historical operation of the linear 3ω sensor is shown in Figs. 1(*b*) and 1(*c*). Figure 1(*b*) shows an instance where the sensor was used to measure the thickness of ice (1 mm thick) with air as a backside boundary condition. The plot shows the output signal (i.e., third harmonic voltage ($V_{3\omega,op}$)) across the heater line measured as a function of frequency. The frequency range is divided into three zones (see inset): zone i refers to the lower frequency range where PD $\sim t_{sample}$ (sample thickness) while zone iii refers to the frequency range where PD $\sim t_{heater}$ (thickness of the heater line). Zone ii refers to a

specific frequency range where $t_{heater} \ll PD \ll t_{sample}$. This frequency range is characterized by a constant $V_{3\omega,op\,avg}$ (avg = average), which is inversely proportional to effective thermal conductivity of the region in the sample and the substrate traversed by the temperature oscillations k_{total} (W/m K). In fact, k_{total} has been derived previously for the 3ω sensor for zone ii as shown in the following equation [32,35]:

$$k_{total} = \frac{\alpha R^2 I^3}{8LV_{3\omega,op\,avg}} \tag{1}$$

where R and L are the resistance (Ω) and length of the heater line (L), respectively; I is the electric current applied across the heater line (A); and $V_{3\omega,op\,avg}$ is the resulting average third harmonic out-of-phase voltage (V) measured from zone ii of the frequency sweep. Finally, the thermal conductivity of the sample can be determined from k_{total} using Eq. (2) [35] if thermal conductivity of the substrate k_{sub} is known beforehand from calibration

$$k_{total} = k_{sample} + k_{sub} \tag{2}$$

Equation (2) is commonly referred to as the boundary mismatch approximation, which assumes that there is no heat transfer through the interface between the substrate and the sample except where the heater line is present. This approximation has been used in the literature to measure thermal conductivity of biological tissues [35,36]. Further, Lubner et al., explains in detail that the error associated with this approximation for the 3ω sensor is usually <5% for cases involving biological tissues [35].

An important feature of the 3ω sensor is that the frequency-dependent measurement enables subsurface sensing of k_{sample} based on the behavior of $V_{3\omega,op}$ in zone ii. In zone i, where $PD \sim t_{sample}$, the behavior of $V_{3\omega,op}$ becomes dependent, not only on k_{sample} but also on t_{sample}, and the backside boundary condition of the sample [43]. This is shown using a representative experiment where the sensor measured ice of 0.5 mm thickness with a varying backside boundary of quasi-thermal copper versus quasi-adiabatic plastic (see Fig. 1(*c*)). Results for thicker ice (0.5–2 mm) with quasi-adiabatic air as backside boundary conditions are shown in a previously reported work [36]. Using these principles, the 3ω sensor on flat and balloon substrates has been used to sense contact with fluid versus tissue, thickness, and freezing phase change.

Numerical Model of 3ω Sensor. The 3ω sensor could be modeled using the transient heat conduction equation

$$k\left[\frac{\partial^2 T'}{\partial x^2} + \frac{\partial^2 T'}{\partial y^2} + \frac{\partial^2 T'}{\partial z^2}\right] = C\frac{\partial T'}{\partial \tau} \tag{3}$$

where T' is the temperature (K) and C is volumetric heat capacity ($J/m^3/K$). The heater line could be modeled as a rectangular surface on a substrate with length L and width b with a periodic heat flux term. However, for longer times (measurement time $\gg 1/\omega$), we can assume a quasi-steady model to reduce the computation time. Mishra et al. developed a two-dimensional axisymmetric finite element quasi-steady model of a thin and infinitely long heater line on a flat substrate [44]. We extend this model here into three-dimensional for the heater line that is serpentine, but attached like the linear heater line onto a flat substrate. Equation (3) is modified for quasi-steady-state by substituting $T'(x,y,z,\tau) = T(x,y,z)e^{i2\omega\tau}$ as shown below:

$$k\left[\frac{\partial^2 T}{\partial x^2} + \frac{\partial^2 T}{\partial y^2} + \frac{\partial^2 T}{\partial z^2}\right] = (i2\omega)CT \tag{4}$$

A commercially available COMSOL package (Version 5.0) was used to simulate the sensor as a quasi-steady model with Eq. (4) as the governing equation. Equation (4) is setup in COMSOL using coefficient form partial differential equation module. The heater line was modeled as a heat source at the surface of the heater line, i.e., negligible thickness as shown in the following equation:

$$k\left[\frac{\partial T}{\partial x} + \frac{\partial T}{\partial y} + \frac{\partial T}{\partial z}\right] = \frac{P}{(L.b)} \quad \text{for } x = 0,\ y = -b/2 \text{ to } +b/2,\ z = 0 \text{ to } +L \tag{5}$$

where P, b, and L are the root mean square (RMS) value of the sinusoidal heating power per unit area of the heater line (W/m^2), width (m), and length (m) of the heater line, respectively. The initial condition is assumed as $T = 0$ for the substrate, sample, and the heater line. Boundary conditions would change depending on specific case scenario as explained later. The thickness is neglected as the PD ($\sim 10\,\mu m$ at 100 Hz for water at 22 °C) $\gg t_{heater}$ (~ 100 nm) for frequencies of interest in biologically relevant materials. Contact resistance between the heater line and the substrate was assumed to be negligible as the values are typically 10^{-8} to 10^{-7} m^2 K/W, which results in an error of <1% in estimation of average temperature of the heater line [35,43,45]. Next, contact resistance between the heater line and the biological samples typically introduces an error of <3% for thermal conductivity measurement and hence were neglected as well [35]. For a given electrical current frequency, the resulting temperature T averaged across the heater line $T_{avg,heater}$ would be determined from the numerical model. This value is then used in Eq. (6) to determine $V_{3\omega,op}$

$$V_{3\omega,op} = \left(-\frac{1}{2}\alpha_T IR\right)\mathrm{Img}(T_{avg,heater}) \tag{6}$$

where α_T, I, and R are the temperature coefficient of resistance (K^{-1}), current (A), and electrical resistance (ohm) across the heater line, respectively. The derivation of Eq. (6) is explained elsewhere [32,46]. The model was validated with closed form analytical solution for linear sensor and also with experimental data for a serpentine heater line on a glass substrate as shown in SI 1 available in the Supplemental Materials on the ASME Digital Collection. Specifically, a gold serpentine sensor of dimensions $b = 5\,\mu m$, $w = 180\,\mu m$, and $L = 0.5$ mm is modeled on a flat glass substrate of (length = 5 mm, width = 5 mm, $t_{sample} = 1$ mm). The backside boundary condition for the experiment was air, i.e., quasi-adiabatic which would approximate the interior of an inflated balloon. Using the numerical model, we first investigated the ability of the sensor to identify ice ($k_{ice} = 2.45$ W/m K, $\alpha_{water} = 1.33 \times 10^{-6}$ m^2/s), water ($k_{water} = 0.6$ W/m K, $\alpha_{water} = 1.43 \times 10^{-7}$ m^2/s), and fat ($k_{fat} = 0.2$ W/m K, $\alpha_{fat} = 1.39 \times 10^{-7}$ m^2/s) at a frequency of 2 Hz, which is in the midfrequency range of zone ii for all the three samples. The heater line was modeled to be on a 2 mm thick glass substrate ($k_{glass} = 1.26$ W/m K; $\alpha_{glass} = 6.6 \times 10^{-7}$ m^2/s) and in contact with the sample of 2 mm thickness. The values for thermal conductivity of ice, water, fat and glass are obtained from the literature at 37 °C [32,47,48]. The backside of the sample and the substrate were assumed to be under adiabatic conditions. The electrical power applied to the heater line was assumed to be 5 mW, which is approximately equal to the heater input power for the serpentine sensor used in the experiments in the paper for an input current of ~10 mA. Typically, a current of 10 mA in the experiments for the given sensor design results in a small temperature rise of <1 K within the tissue/glass substrate, which minimizes transient heating of the substrate/tissue and on the other hand provides an output $V_{3\omega,op}$ with high signal to noise ratio (>10). Next, the ability of the serpentine sensor to measure thickness was investigated. For thickness, the sensor was modeled to be in contact with ice with water or fat as backside boundary conditions in the thickness range of 0.5–2 mm range. The resulting $V_{3\omega,op}$ is determined at 0.1 Hz and plotted as a function of thickness of the sample. The frequency of 0.1 Hz is chosen as the corresponding PD (~0.33 mm in fat, ~0.34 mm in

water, ~1.03 mm in ice) is comparable to the thickness of 0.5–2 mm for PV and lies in zone i (low frequency range).

Finally, we investigated the ability of the sensor to sense phase change from water to ice. This is achieved by first modeling the serpentine sensor to be in contact with water with an adiabatic backside boundary condition. Next, $V_{3\omega,op}$ at 2 Hz is determined and plotted as a function of t_{ice}/t_{water} by changing the thickness of ice (i.e., ice front is advancing next to the sensor). The frequency of 2 Hz is chosen as the corresponding PD is ~0.074 mm for fat, ~0.075 mm for water, 0.23 mm for ice, which is an order of magnitude less than the thickness of 2 mm that we wish to sense within PV and lies in zone ii of both ice and water.

Microthermal Sensing Using the Serpentine Sensor on a Flat Substrate

Construction of the Serpentine Sensor. A gold serpentine-shaped heater line ($L = 0.5$ mm, $b = 5$ μm, $w = 180$ μm, $t_{heater} = 100$ nm) is patterned onto a 1 mm thick silica glass (amorphous SiO_2) substrate using standard photolithography and lift off techniques. A chromium layer (~5 nm thick) is used as an adhesion to bond gold line onto glass substrate. A polystyrene dielectric layer (~1 μm thick) is deposited on top of the heater line. The process is detailed elsewhere [36]. The glass substrate is attached on top of another silica glass substrate (1 mm thick). The heater lines are connected to the signal processing unit using copper wires.

Data Acquisition From the 3ω Sensor. The sensor is excited with an alternating current produced at a fixed frequency by a custom voltage to current circuit. This input current is driven by the reference output of a lock-in amplifier (SR 830, Stanford Research Systems, Sunnyvale, CA). The frequency of the input current can be controlled using the lock-in amplifier. The output signal from the sensor comprises a 1ω and a 3ω component, which is separated using a multiplying digital-to-analog converter. The lock-in amplifier was then used to record the $V_{1\omega}$ and $V_{3\omega}$ signal. The amplifier can be adjusted for optimum time constant (response time) and voltage sensitivity in the output signal.

Sensing Contact. Agargel and mouse liver are chosen as surrogate tissues to pulmonary vein as their thermal conductivity (~0.5 W/m K for liver and 0.6 W/m K for agargel) at 37 °C show a similar increase on freezing to −40 °C (~1.7 W/m K for liver and 2.63 W/m K for agargel) as shown in PV (0.57 W/m K at 37 °C and 1.44 W/m K at −40 °C) [36,47]. Our experimental setup consists of a supported 3ω sensor with a serpentine-shaped heater line ($L = 0.5$ mm, $b = 5$ μm, $w = 180$ μm, $t_{heater} = 100$ nm), a piece of tissue, and a variable speed peristaltic pump (Cole-Parmer Masterflex®, Vernon Hills, IL) used to control flow over the sensor. To verify our ability to sense probe contact, we used the sensor to differentiate between tissue contact and flow conditions. Here, the tissue was a mouse liver immersed in phosphate buffer solution and stored in a 4 °C refrigerator. All biological tissues were used for experiments within 24 h of harvesting animals used for other purposes. Tissues were placed on a recessed surface of known depth and sliced using a microtome blade. Thicknesses between 0.5 and 2 mm were then confirmed using thickness gauge (Mitotoya™, Sakado, Japan) with an accuracy of ±0.1 mm. For sensing water flow, the peristaltic pump was used to control water flow over the sensor at a certain speed. For sensing tissue contact, the mouse liver was manually placed on top of the sensor, thereby blocking the water flow. The sensor recorded the $V_{3\omega,op}$ at a fixed frequency of 10.1 Hz (constant PD) and input RMS current of 10 mA. A lock-in time constant of 3 s was selected as a compromise between measurement noise and time response of the measurement system. The chosen frequency is a typical value for which PD (~0.034 mm for mouse liver) $\ll t_{sample}$ (~2 mm).

Sensing Tissue Thickness. Agargel of known thickness was prepared by dissolving 0.5% weight of agarose in water. The solution is then filled into a space between glass plates separated by a known distance. Then the fixture is stored in a refrigerator for 6 h to form agargel. Thickness was confirmed using a thickness gauge (Mitotoya™, Sakado, Japan). Agargel was placed on the sensor and immediately frozen to −25 °C using a cooler enclosed in a cryofreezer (Planer Kryo 10 Series III, Middlesex, UK). For an input RMS current of 10 mA, $V_{3\omega,op}$ was recorded as a function of frequency (from 0.1 to 10 Hz) at a fixed temperature of −25 °C on the sensor surface. The experiment was repeated for a different thickness ($n = 3$) of frozen agargel (i.e., changed from ~0.5 mm to ~1.9 mm) while keeping the backside boundary condition as air ($k_{air} \sim 0.02$ W/m K) at −55 °C [49]. The thermal convection effects of air can be assumed negligible as the convection heat loss is <1% of the conduction heat flow from the heater line if convection coefficient is assumed to be <25 W/m^2 K [43].

Sensing Phase Change. A 3 mm thick, several cm long mouse liver slice was placed on the sensor. The temperature was lowered from 20 °C to −10 °C, allowing the tissue sample to become frozen. After allowing the freezing event to complete and the voltage to stabilize, the temperature was increased back to 20 °C. Completion of freezing and thawing events were verified by visual inspection during the experiment. An alternating current with an RMS of 10 mA at a frequency of 10.1 Hz, which is in the zone ii of the frequency sweep, was applied across the sensor, and the results were recorded with a lock-in time constant of 3 s.

Microthermal Sensing Using Serpentine Sensors on a Balloon Substrate

Integration of Serpentine 3ω Sensor Onto a Balloon. The 3ω sensors were deposited on flexible balloons [38–41]. Specifically, the 3ω sensors and associated interconnects/contacts were microfabricated on silicon wafers using conventional microfabrication techniques. An initial sacrificial layer of poly(methyl methacrylate) spun onto the wafer allowed eventual release of the entire 3ω device from the wafer. Elastomeric transfer printing techniques were then used to transfer the device from the wafer to a balloon surface. The device contains gold lines, deposited by electron-beam evaporation and interconnects by photolithography, fully encapsulated in thin layers of polyimide (spin cast). Careful design of the polyimide geometries provided the required mechanical robustness (to withstand the pressure of the balloon) as well as encapsulation from surrounding fluids as previously described for other flexible electronic constructs [39–42].

Sensing Contact. The following experiments were conducted using a 3ω sensor of serpentine shaped heater line ($L = 0.5$ mm, $b = 5$ μm) integrated onto a balloon. To verify our ability to sense probe contact, we used a sensor integrated onto a balloon to differentiate between contact with agargel and air. The balloon was positioned a few mm away from the agargel (2 mm thick), which in turn was placed on a copper plate at room temperature (~22 °C). The sensor recorded the $V_{3\omega,op}$ at a fixed frequency of 11.1 Hz (constant PD) and input RMS current of 6 mA. A lock-in time constant of 3 s was selected as a compromise between measurement noise and time response of the measurement system. The chosen frequency is a typical value for which PD (~0.032 mm for agargel) $\ll t_{sample}$ (zone ii) as the purpose is to sense the tissue that is in immediate contact with the sensor. The balloon was moved so that the sensor came in contact with the agargel.

Sensing Tissue Thickness. A copper plate was positioned inside a cryofreezer (Planer Kryo 10 Series III, Middlesex, UK) equilibrated to −25 °C. Agargel (0.5% weight of agarose in water) was placed on the copper plate (5 mm thick) at −25 °C and immediately frozen. The sensor on the balloon was brought in contact with the top surface of the agargel. Next, for an input RMS current of 6 mA, $V_{3\omega,op}$ was recorded at 0.1 Hz at a fixed temperature of −25 °C on the sensor surface. Here, the chosen frequency is a typical value for which PD ~ t_{sample} as the purpose is to sense the backside of the sample in contact with the sensor. The experiment

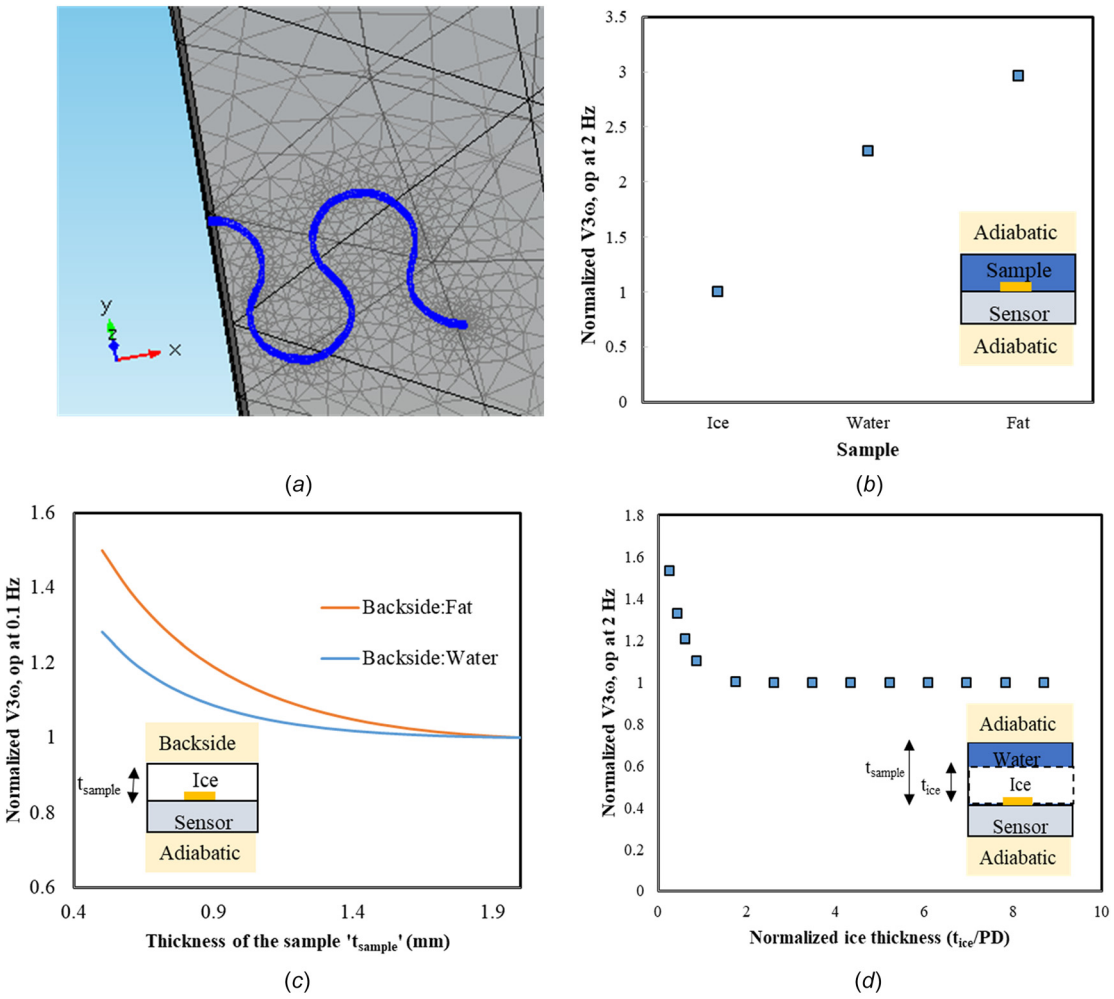

Fig. 2 Finite element analysis of the serpentine sensor ($L = 0.5$ mm, $b = 5$ μm, $w = 180$ μm) on a flat substrate: (*a*) three-dimensional numerical discretization of the serpentine sensor on a flat 2 mm thick glass substrate. (*b*) Numerical predictions of $V_{3\omega,op}$ at 2 Hz for different samples of ice, water, and fat in contact with the sensor. $V_{3\omega,op}$ is normalized to the values of ice. (*c*) Numerical predictions of $V_{3\omega,op}$ at 0.1 Hz for varying sample thickness of ice with water or fat on the backside. $V_{3\omega,op}$ for each configuration is normalized to the values for samples at 2 mm thickness. (*d*) Numerical predictions of $V_{3\omega,op}$ at 2 Hz for varying thickness of ice as ice front moves from the sensor. $V_{3\omega,op}$ is normalized to the PD in ice.

was repeated for different thickness of frozen agargel (i.e., changed from ~0.5 mm to ~2.0 mm) while keeping the backside boundary condition as copper ($k_{copper} \sim 386$ W/m K) [48].

Sensing Phase Change. A 3 mm thick sample of agargel was placed on the copper plate at 20 °C. The sensor on the balloon was brought in contact with the top surface of the agargel. The temperature of the copper plate was lowered from 20 °C to −25 °C, freezing the agargel sample. After the cooling process is complete and followed by voltage stabilization, the temperature was increased back to 20 °C. An alternating current with an RMS of 6 mA at a frequency of 11.1 Hz, which is in the zone ii of the frequency sweep, was applied across the sensor.

Results and Discussion

Numerical Characterization of Serpentine 3ω Sensors on a Flat Substrate. The 3ω sensors had to be modified from a linear into a serpentine shape for deposition onto a balloon substrate. However, the serpentine shape changes the behavior of sensor output signal, $V_{3\omega,op}$ as a function of frequency. So, a numerical model as shown in Fig. 2(*a*) was created to confirm the ability of the serpentine shaped sensor for microthermal sensing. First, the ability of the sensor to differentiate between biologically relevant materials such as fat, water, and ice is shown in Fig. 2(*b*). Here, $V_{3\omega,op}$ is determined for cases where the sample was in contact with fat, water, and ice. $V_{3\omega,op}$ was normalized with $V_{3\omega,op}$ obtained for ice ($k_{ice} = 2.45$ W/m K). The value increases to ~2.3 for water with $k_{water} = 0.6$ W/m K and ~3.0 for fat with $k_{fat} = 0.2$ W/m K [47]. The reason $V_{3\omega,op}$ increases with drop in thermal conductivity could be explained by Eqs. (1) and (2). For the same sensor (substrate and heater line geometry) and input electrical current, $V_{3\omega,op}$ measured at a frequency in zone ii, i.e., 2 Hz, is inversely proportional to thermal conductivity. Thus, if the sensor and input current remain the same, the sensor can be used to sense contact with different materials through $V_{3\omega,op}$.

Next, the ability of the sensor to sense thickness of materials such as water and ice with different boundary conditions was modeled as shown in Fig. 2(*c*). Here, $V_{3\omega,op}$ is normalized for each case with the value determined at 2 mm. For the case with ice as sample and fat as backside, normalized $V_{3\omega,op}$ increases to ~1.03 for 1.5 mm thick sample, ~1.15 for 1 mm thick sample, and finally ~1.50 for 0.5 mm thick sample. In contrast, for the case with water as backside boundary, the normalized $V_{3\omega,op}$ increases to ~1.01 for 1.5 mm thick sample, ~1.06 for 1 mm thick sample, and finally ~1.28 for 0.5 mm thick sample. If the noise in the signal is less than 1%, the sensor can be reliably used to sense thickness even up to 2 mm for ice with fat as backside boundary.

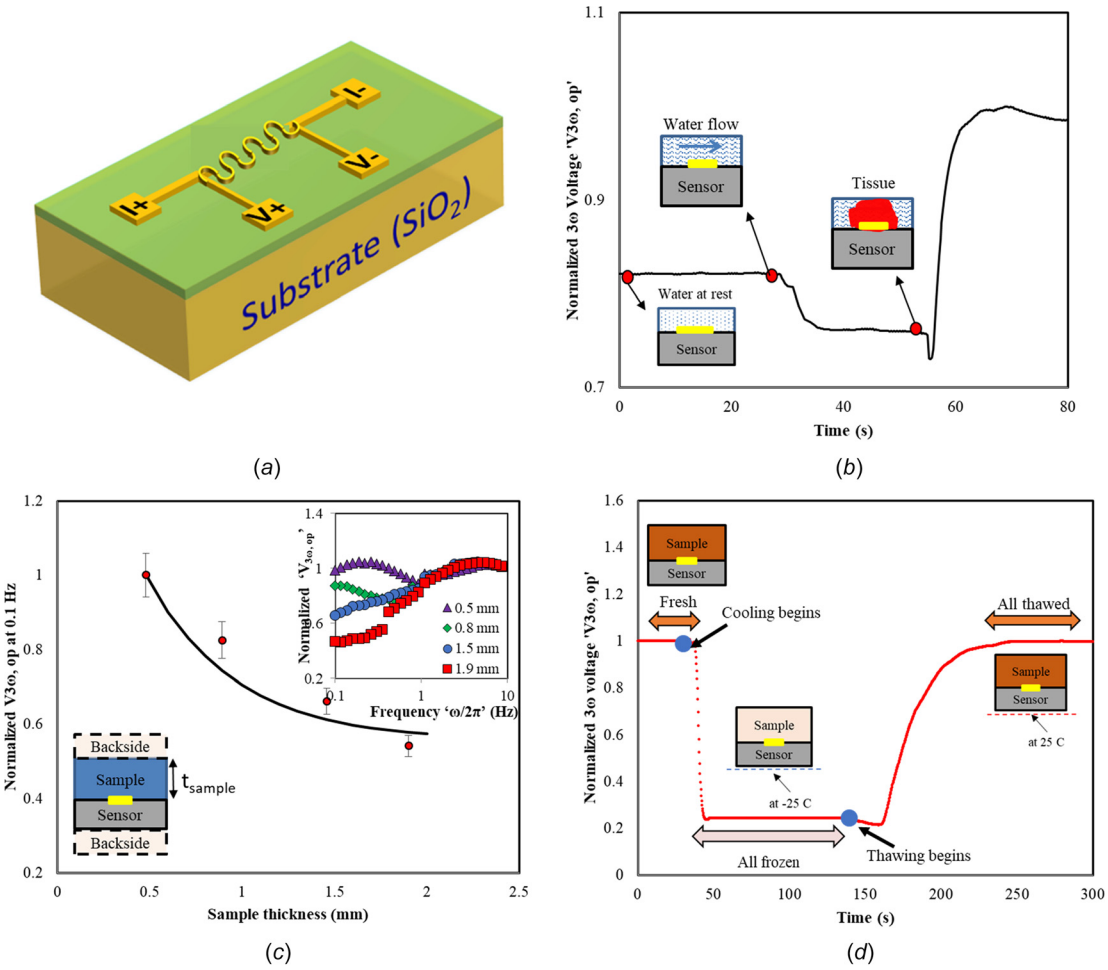

Fig. 3 Microthermal sensing using a serpentine shaped sensor ($L = 0.5$ mm, $b = 5\,\mu$m, $w = 180\,\mu$m, $t_{heater} = 100$ nm) on a flat substrate: (*a*) Serpentine-shaped sensor on a flat glass substrate. (*b*) (Contact) Experimental measurement of water versus tissue contact; $V_{3\omega,op}$ is measured at ω of 10.1 Hz. (*c*) (Thickness) Experimental measurement of $V_{3\omega,op}$ at 0.1 Hz for different thickness of frozen agargel at −25 °C (AVG ± standard deviation of $N = 3$). Black line shows the results from the numerical model. The backside boundary conditions are air and modeled as adiabatic conditions. $V_{3\omega,op}$ is normalized to its value for 0.5 mm thick sample. Inset shows experimental measurement of $V_{3\omega,op}$ as a function of frequency for different sample thickness. (*d*) (Phase change) Experimental measurement of $V_{3\omega,op}$ during mouse liver freezing at 10.1 Hz and normalized to its initial value at 0 s. Cooling begins at ∼30 s and thawing begins at ∼140 s.

Finally, the ability of the sensor to sense water to ice phase change as a function of normalized ice thickness is shown in Fig. 2(*d*). Specifically, we show that the sensor can differentiate the end points of the phase change event, i.e., frozen versus unfrozen and to provide a qualitative trend of $V_{3\omega,op}$ due to k changes during solidification in a water droplet. Figure 2(*d*) shows that $V_{3\omega,op}$ decreases by 60% as the sample goes from partial to total solidification. As Eq. (4) is quasi-steady, there was no need to add any effects due to latent heat. $V_{3\omega,op}$ is determined at 2 Hz as it is in zone ii and scales with t_{sample} and is independent of backside boundary conditions. $V_{3\omega,op}$ is normalized to the PD in ice. As the thickness ratio (t_{ice}/PD) increases to 1.73, normalized $V_{3\omega,op}$ decreases to ∼1 beyond which there is a plateau in the signal. This sharp drop in the signal is due to the fact that the thermal conductivity of ice is at 2.45 W/m K, which is ∼4 times that of water at 0.6 W/m K thereby confirming the ability of the sensor to measure a phase change event.

While the sensor operates as desired, the original ability of the 3ω sensor to measure k_{sample} of materials such as ice, water, and fat using $V_{3\omega,op}$ in Eq. (1) will be degraded. More specifically, the current form factor of the serpentine shaped heater line introduces errors while using Eq. (1) as it was originally derived for linear sensors. The error can be minimized by changing the form factor as explained in SI 4.2 available in the Supplemental Materials on the ASME Digital Collection; however, thermal conductivity errors with the current form factor to measure ice can be as high as 115%. Alternatively, finite element analysis (using COMSOL) can be used to back calculate thermal conductivity from experimentally measured $V_{3\omega,op}$ if sufficient output third harmonic voltage is available as a function of frequency for comparison [37].

As the sensor would eventually be integrated onto a balloon substrate, the effect of size of the balloon (i.e., radius of curvature) on the sensor performance was investigated in SI.4.2 available in the Supplemental Materials on the ASME Digital Collection. The error in $V_{3\omega,op}$ over a wide frequency range of 0.1 to 1000 Hz and k_{sample} is found to be negligible for the current application, where the heater line on the balloon will bend around a radius equal to the ostium of the pulmonary vein (∼4 to 6 mm) [50].

Microthermal Sensing Using the Serpentine Sensor on a Flat Substrate. After construction of the serpentine 3ω sensor on a flat, glass substrate as shown in Fig. 3(*a*), a number of specific experimental measurements were undertaken. First, we used the sensor to differentiate between tissue contact and flow conditions as shown in Fig. 3(*b*). Here, the 3ω voltage ($V_{3\omega,op}$) is shown to be constant as the water is at rest and then drops at ∼28 s due to flow

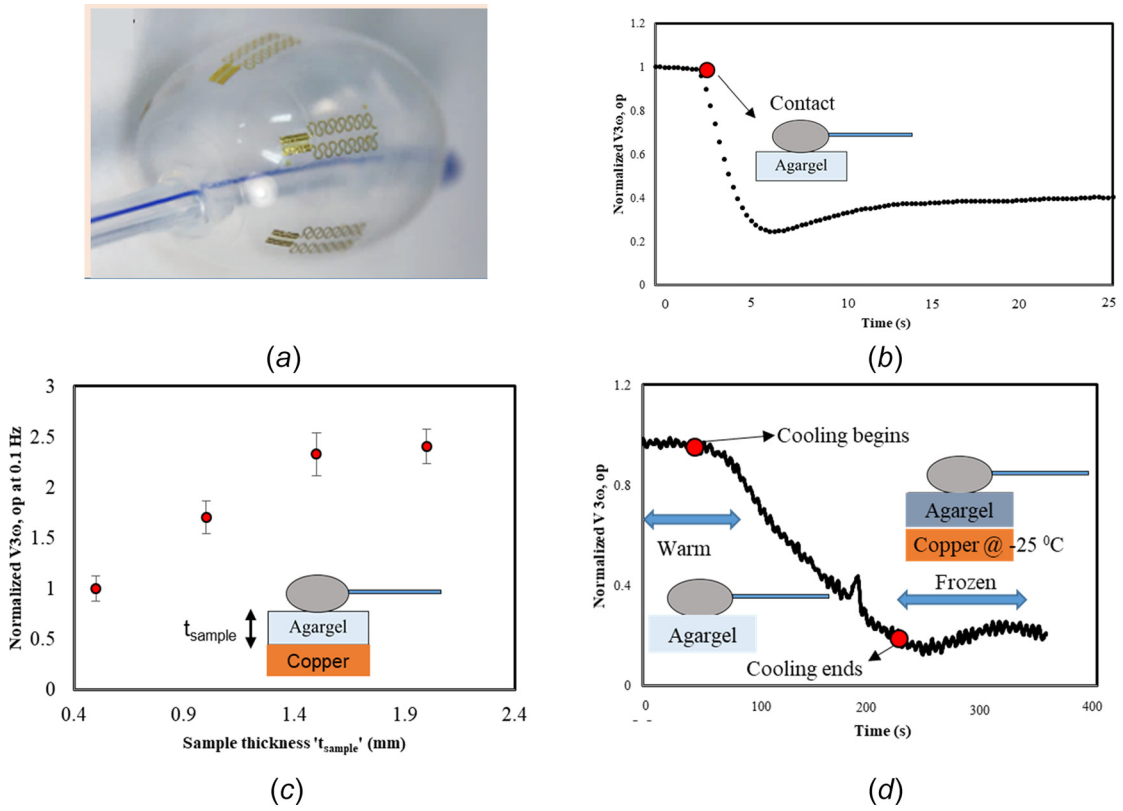

Fig. 4 Microthermal sensing using serpentine shaped sensor ($L = 0.5$ mm, $b = 5\ \mu$m, $w = 180\ \mu$m, $t_{heater} = 100$ nm) on a balloon substrate: (*a*) 3ω sensor deposited on a balloon. (*b*) (Contact) Experimental measurement of $V_{3\omega,op}$ as a function of time at 11.1 Hz heater electrical frequency. The sensor is brought in contact with agargel at ~2 s and $V_{3\omega,op}$ is normalized to its initial value recorded in air. (*c*) (Thickness) Experimental measurement of $V_{3\omega,op}$ as a function of sample thickness d measured at ω of 0.1 Hz (AVG ± standard deviation of $N = 3$). $V_{3\omega,op}$ is normalized to its value for 0.5 mm thick sample. (*d*) (Phase change) Experimental measurement of $V_{3\omega,op}$ at 11.1 Hz and normalized to its initial value when the sensor is in contact with agargel. Cooling begins at ~90 s and ends at ~240 s.

and concomitant convective heat loss. At 50 s, the plot shows that placing a piece of low k tissue (1 mm thick mouse liver) on top of the sensor replaces water flow with tissue contact thereby increasing $V_{3\omega,op}$ to the highest value of all cases. Figure 3(*c*) shows $V_{3\omega,op}$ at 0.1 Hz as a function of sample thickness normalized to its value for 0.5 mm thick sample. The black line represents the results from numerical modeling of the sensor in contact with frozen agargel. The inset figure shows normalized $V_{3\omega,op}$ as a function of frequency for varying sample thickness. At high frequencies, the thermal penetration depth (PD = $(\alpha/2\omega)^{0.5}$) is small and stays within the sample as depicted in the inset. However, at lower frequencies, the penetration depth can increase to become comparable to the sample thickness. More specifically, the $V_{3\omega,op}$ response at 0.1 Hz decreases with increasing thickness (0.5 to 2 mm). Finally, the ability to sense phase change was verified by monitoring $V_{3\omega,op}$ during freezing and thawing of a mouse liver placed on top of the sensor as shown in Fig. 3(*d*). The temperature of the stage below the sensor was changed to −25 °C at ~30 s, after which there was a drop in $V_{3\omega,op}$. This drop corresponds to the jump in k for biological tissues on freezing and is followed by a stable region where the sample is completely frozen. After ~140 s, the temperature of the stage is set to 15 °C, resulting in increase in $V_{3\omega,op}$.

Integration of Serpentine 3ω Sensor Onto a Balloon. Linear 3ω sensors (Fig. 1(*a*)) have been used to sense contact with tissue versus water, thickness, and phase change [36]. However, this linear heater line sensor cannot be integrated onto a flexible, stretchable substrate such as a cryoballoon as it fractures under the large deformations needed to inflate the balloon. Hence, we modified the heater line into a serpentine shape that allows in- and out-of-plane buckling motion under large deformations. Such 3ω sensors have been previously developed to measure thermal conductivity on the surface of human skin [37]. The sensors shown in Fig. 4(*a*) involve a small Au heater with $b = 5\ \mu$m, width $w = 180\ \mu$m, and length $L = 0.5$ mm and a similarly shaped pair of polyimide encapsulation layers with widths of 20 μm. An overall layout in the form of a filamentary serpentine structure provides elastic stretchability of 54% and 71% in the horizontal and vertical directions, respectively, as computed by numerical analysis with a threshold for Au plastic deformation of 0.3% [37].

Microthermal Sensing Using Serpentine Sensors on a Balloon Substrate. In Fig. 4(*a*), the serpentine sensor is deployed on a balloon to sense contact, thickness, and phase change. Figure 4(*b*) shows 3ω voltage at rest and then the response at ~2 s when it is brought in contact with agargel (0.5% weight of agarose in water) which results in an immediate drop in $V_{3\omega,op}$ due to high k for agargel versus air. Next, to verify our ability to measure thickness, we prepared several samples of thin frozen agargel of varying thickness and recorded the 3ω signal at 0.1 Hz (Fig. 4(*c*)). $V_{3\omega,op}$ at 0.1 Hz (which has a PD ~ 2 mm in ice) increases as a function of thickness (0.5 to 2 mm). In contrast, $V_{3\omega,op}$ at 0.1 Hz decreased with increase with thickness for the flat substrate. This difference is due to the fact that the backside boundary condition for the balloon experiments is highly conductive copper plate while that of flat substrate experiments is highly insulating air ($k = 0.02$ W/m K). Finally, we used the sensor to monitor freezing of agargel through its effect on the 3ω voltage as shown in Fig. 4(*d*). $V_{3\omega,op}$ is normalized with respect to its initial value where the agargel is

Table 1 Summary of measurement parameters used to record 3ω signal ($V_{3\omega,op}$) from the 3ω sensor using a lock-in amplifier

Characteristics of the sensor		Linear sensor on flat substrate	Serpentine sensor on flat substrate	Serpentine sensor on balloon
Data discussed		Figure 1 and Natesan et al. [36]	Figure 3	Figure 4
Size of the heater line		$L = 2$ mm, $b = 20$ μm, $t_{heater} = 100$ nm	$L = 0.5$ mm, $b = 5$ μm, $w = 180$ μm, $t_{heater} = 100$ nm	$L = 0.5$ mm, $b = 5$ μm, $w = 180$ μm, $t_{heater} = 100$ nm
Substrate		Glass (~1 mm thick)	Glass (~1 mm thick)	Polyurethane balloon (~0.1 mm thick)
Contact	Measurement	Water versus mouse liver tissue	Water versus mouse liver tissue	Air versus agargel
	Response time[a]	1 s	3 s	3 s
Thickness	Measurement	Agargel: 0.5–2.0 mm thick	Agargel: 0.5–1.9 mm thick	Agargel: 0.5–2.0 mm thick
	Waiting time[b]	15 min	15 min	15 min
Phase	Measurement	Freezing and thawing of mouse liver and agargel	Freezing and thawing of mouse liver	Freezing and thawing of agargel
	Response time[a]	1 s	3 s	3 s

[a]Response time (RT) refers to the time constant used for the lock-in amplifier during the measurement.
[b]Waiting time refers to the time waited before voltage stabilization (<1% noise), which was ~30*RT.

not frozen. Here the temperature of the copper plate below the sample was changed to −25 °C at ~90 s after which there was a drop in $V_{3\omega,op}$. This drop corresponds to the jump in k for agargel on freezing and is followed by a region where the sample is completely frozen.

The benchtop experiments show that the serpentine sensor deployed on a balloon could be used to determine contact with tissue versus flowing water (Fig. 3(*b*)) or air versus agargel (Fig. 4(*b*)). Specifically, Fig. 3(*b*) shows that the signal changes by ~16% between flowing water and tissue, while the signal to noise ratio is usually >10 suggesting that the sensitivity is sufficient to sense tissue contact. This ability could translate into an application where the sensor could detect if the balloon is in contact with the tissue of interest (PV for atrial fibrillation). Initially, as the balloon is not in contact but positioned near PV, blood will flow over the sensor. As shown in Fig. 3(*b*) with water, the convective heat transfer from blood will lead to a low value of $V_{3\omega,op}$. On the other hand, if PV is occluded, the sensor will come in contact with the tissue represented by an increase in $V_{3\omega,op}$. Thus, the sensor can be used to detect occlusion of PV. Next, the ability of the sensor to detect thickness is shown in Fig. 4(*c*). Specifically, Fig. 4(*c*) shows that we can sense thickness of agargel with a resolution of 0.5 mm. Similarly, the sensor can be calibrated to detect the thickness of PV after the sensor is in contact. First, the sensor could be used at a high frequency (zone ii), where the thermal conductivity of PV ($k_{PV,in\ vivo}$) could be measured. Next, Fig. 4(*c*) could be used to determine the expected $V_{3\omega,op}$ at 0.1 Hz for different thickness of PV. Finally, the ability of the sensor to detect freezing phase change as shown in Fig. 4(*d*) could be used to detect the freezing of PV. The signal changes by 70% as the agargel freezes down implying a strong sensitivity to solidification likely due to thermal conductivity increasing dramatically.

Summary

In summary, we have shown how to modify a linear 3ω sensor for use on a balloon using a serpentine heater line and flexible electronic approaches (Fig. 1). First, we numerically studied the behavior of the serpentine sensor on a flat substrate for different materials of varying thickness (Fig. 2). Then, we explored the error introduced by curvature of the substrate (SI 2 available in the Supplemental Materials on the ASME Digital Collection). Next, we show experimental measurements of serpentine sensors on flat substrates for sensing contact, thickness, and phase change within thin biological tissues at the limit of resolution of clinical imaging, 0.5–2 mm (Fig. 3). Finally, we demonstrate experimental proof of principle that we can integrate the sensor onto a balloon and make similar measurements (Fig. 4). A summary of these experimental results is tabulated in Table 1. The response time refers to the parameter used by the lock-in amplifier during the measurement. The response time for contact and phase change measurement is of the order of 1–3 s, while the waiting time for the voltage to stabilize for thickness measurements was up to 15 min. This was due to the necessity of acquiring a reliable signal at low frequency of 0.1 Hz which could benefit from improved electronics thereby reducing the waiting time in the future.

In addition to improving balloon-based thermal or focal treatment in PV as envisioned here, the new thin, flexible sensor could be used on other probes or balloons for monitoring thermal (heat or cold) focal therapy in peripheral artery disease, renal or hepatic artery treatments (hypertension and diabetes) in the future. Conceivably these sensors can also be used on balloons using a non-thermal ablation technique (such as irreversible electroporation) for accurate placement of electrodes to achieve a desired ablation zone [51,52].

Acknowledgment

Funding from a Minnesota Biotechnology Partnership grant, Doctoral Dissertation Fellowship (2016/17), and the use of the Nano-Center at University of Minnesota are gratefully acknowledged. Inputs from Prof. Chris Dames and Wyatt Hodges from University of California on modeling the 3ω sensor are gratefully acknowledged.

Funding Data

- Minnesota Biotechnology Partnership grant, Doctoral Dissertation Fellowship (2016/17), and the use of the Nano-Center at University of Minnesota (Funder ID: 10.13039/100007249).

References

[1] Chu, K. F., and Dupuy, D. E., 2014, "Thermal Ablation of Tumours: Biological Mechanisms and Advances in Therapy," Nat. Rev. Cancer, **14**(3), pp. 199–208.
[2] He, X., and Bischof, J. C., 2003, "Quantification of Temperature and Injury Response in Thermal Therapy and Cryosurgery," Crit. Rev. Biomed. Eng., **31**(5&6), p. 31.
[3] Hoffmann, N. E., and Bischof, J. C., 2002, "The Cryobiology of Cryosurgical Injury," Urology, **60**(2), pp. 40–49.
[4] Andreano, A., and Brace, C. L., 2013, "A Comparison of Direct Heating During Radiofrequency and Microwave Ablation in Ex Vivo Liver," Cardiovasc. Interventional Radiol., **36**(2), pp. 505–511.
[5] Bruce, C. J., Packer, D. L., and Seward, J. B., 1999, "Intracardiac Doppler Hemodynamics and Flow: New Vector, Phased-Array Ultrasound-Tipped Catheter," Am. J. Cardiol., **83**(10), pp. 1509–1512.
[6] Onik, G. M., Cohen, J. K., Reyes, G. D., Rubinsky, B., Chang, Z., and Baust, J., 1993, "Transrectal Ultrasound-Guided Percutaneous Radical Cryosurgical Ablation of the Prostate," Cancer, **72**(4), pp. 1291–1299.
[7] Onik, G., Rubinsky, B., Zemel, R., Weaver, L., Diamond, D., Cobb, C., and Porterfield, B., 1991, "Ultrasound-Guided Hepatic Cryosurgery in the Treatment of Metastatic Colon Carcinoma. Preliminary Results," Cancer, **67**(4), pp. 901–907.

[8] Gilbert, J. C., Onik, G. M., Hoddick, W. K., and Rubinsky, B., 1985, "Real Time Ultrasonic Monitoring of Hepatic Cryosurgery," Cryobiology, **22**(4), pp. 319–330.

[9] Onik, G., Cooper, C., Goldberg, H. I., Moss, A. A., Rubinsky, B., and Christianson, M., 1984, "Ultrasonic Characteristics of Frozen Liver," Cryobiology, **21**(3), pp. 321–328.

[10] Sandison, G. A., Loye, M. P., Rewcastle, J. C., Hahn, L. J., Saliken, J. C., McKinnon, J. G., and Donnelly, B. J., 1998, "X-Ray CT Monitoring of Iceball Growth and Thermal Distribution During Cryosurgery," Phys. Med. Biol., **43**(11), pp. 3309–3324.

[11] Schwartz, B. F., Rewcastle, J. C., Powell, T., Whelan, C., Manny, T., Jr., and Vestal, J. C., 2006, "Cryoablation of Small Peripheral Renal Masses: A Retrospective Analysis," Urology, **68**(1), pp. 14–18.

[12] Shenoi, M. M., Zhang, X., Venkatasubramanian, R. T., Grassl, E. D., George, L., Schmechel, S., Coad, J. E., and Bischof, J. C., 2009, "CT Visualization and Histopathological Assessment of Cryoablation in Pulmonary Veins," ASME Paper No. SBC2009-206640.

[13] Butts, K., Sinclair, J., Daniel, B. L., Wansapura, J., and Pauly, J. M., 2001, "Temperature Quantitation and Mapping of Frozen Tissue," J. Magn. Reson. Imaging, **13**(1), pp. 99–104.

[14] Daniel, B. L., Butts, K., and Block, W. F., 1999, "Magnetic Resonance Imaging of Frozen Tissues: Temperature-Dependent MR Signal Characteristics and Relevance for MR Monitoring of Cryosurgery," Magn. Reson. Med., **41**(3), pp. 627–630.

[15] Gilbert, J. C., Rubinsky, B., Roos, M. S., Wong, S. T. S., and Brennan, K. M., 1993, "MRI-Monitored Cryosurgery in the Rabbit Brain," Magn. Reson. Imaging, **11**(8), pp. 1155–1164.

[16] Pease, G. R., Wong, S. T. S., Roos, M. S., and Rubinsky, B., 1995, "Mr Image-Guided Control of Cryosurgery," J. Magn. Reson. Imaging, **5**(6), pp. 753–760.

[17] Wansapura, J. P., Daniel, B. L., Vigen, K. K., and Butts, K., 2005, "In Vivo MR Thermometry of Frozen Tissue Using R2* and Signal Intensity1," Acad. Radiol., **12**(9), pp. 1080–1084.

[18] Haïssaguerre, M., Gencel, L., Fischer, B., Le Métayer, P., Poquet, F., Marcus, F. I., and Clémenty, J., 1994, "Successful Catheter Ablation of Atrial Fibrillation," J. Cardiovasc. Electrophysiol., **5**(12), pp. 1045–1052.

[19] Avitall, B., Urboniene, D., Rozmus, G., Lafontaine, D., Helms, R., and Urbonas, A., 2003, "New Cryotechnology for Electrical Isolation of the Pulmonary Veins," J. Cardiovasc. Electrophysiol., **14**(3), pp. 281–286.

[20] Kuck, K.-H., and Fürnkranz, A., 2010, "Cryoballoon Ablation of Atrial Fibrillation," J. Cardiovasc. Electrophysiol., **21**(12), pp. 1427–1431.

[21] Kojodjojo, P., O'Neill, M. D., Lim, P. B., Malcolm-Lawes, L., Whinnett, Z. I., Salukhe, T. V., Linton, N. W., Lefroy, D., Mason, A., Wright, I., Peters, N. S., Kanagaratnam, P., and Davies, D. W., 2010, "Pulmonary Venous Isolation by Antral Ablation With a Large Cryoballoon for Treatment of Paroxysmal and Persistent Atrial Fibrillation: Medium-Term Outcomes and Non-Randomised Comparison With Pulmonary Venous Isolation by Radiofrequency Ablation," Heart, **96**(17), pp. 1379–1384.

[22] Haeusler, K. G., Koch, L., Ueberreiter, J., Endres, M., Schultheiss, H.-P., Heuschmann, P. U., Schirdewan, A., and Fiebach, J. B., 2010, "Stroke Risk Associated With Balloon Based Catheter Ablation for Atrial Fibrillation: Rationale and Design of the MACPAF Study," BMC Neurol., **10**(1), p. 63.

[23] Reddy, V. Y., Neuzil, P., Themistoclakis, S., Danik, S. B., Bonso, A., Rossillo, A., Raviele, A., Schweikert, R., Ernst, S., Kuck, K.-H., and Natale, A., 2009, "Visually-Guided Balloon Catheter Ablation of Atrial Fibrillation Experimental Feasibility and First-in-Human Multicenter Clinical Outcome," Circulation, **120**(1), pp. 12–20.

[24] Doppalapudi, H., Yamada, T., and Kay, G. N., 2009, "Complications During Catheter Ablation of Atrial Fibrillation: Identification and Prevention," Heart Rhythm, **6**(12), pp. S18–S25.

[25] Calkins, H., Reynolds, M. R., Spector, P., Sondhi, M., Xu, Y., Martin, A., Williams, C. J., and Sledge, I., 2009, "Treatment of Atrial Fibrillation With Antiarrhythmic Drugs or Radiofrequency Ablation Two Systematic Literature Reviews and Meta-Analyses," Circ.: Arrhythmia Electrophysiol., **2**(4), pp. 349–361.

[26] Haíssaguerre, M., Jaís, P., Shah, D. C., Gencel, L., Pradeau, V., Garrigues, S., Chouairi, S., Hocini, M., Le Métayer, P., Roudaut, R., and Clémenty, J., 1996, "Right and Left Atrial Radiofrequency Catheter Therapy of Paroxysmal Atrial Fibrillation," J. Cardiovasc. Electrophysiol., **7**(12), pp. 1132–1144.

[27] Malmborg, H., Lönnerholm, S., and Blomström-Lundqvist, C., 2008, "Acute and Clinical Effects of Cryoballoon Pulmonary Vein Isolation in Patients With Symptomatic Paroxysmal and Persistent Atrial Fibrillation," Europace, **10**(11), pp. 1277–1280.

[28] Ahmed, H., Neuzil, P., d'Avila, A., Cha, Y.-M., Laragy, M., Mares, K., Brugge, W. R., Forcione, D. G., Ruskin, J. N., Packer, D. L., and Reddy, V. Y., 2009, "The Esophageal Effects of Cryoenergy During Cryoablation for Atrial Fibrillation," Heart Rhythm, **6**(7), pp. 962–969.

[29] Kuck, K.-H., Fürnkranz, A., Chun, K. R. J., Metzner, A., Ouyang, F., Schlüter, M., Elvan, A., Lim, H. W., Kueffer, F. J., Arentz, T., Albenque, J.-P., Tondo, C., Kühne, M., Sticherling, C., and Brugada, J., 2016, "Cryoballoon or Radiofrequency Ablation for Symptomatic Paroxysmal Atrial Fibrillation: Reintervention, Rehospitalization, and Quality-of-Life Outcomes in the FIRE AND ICE Trial," Eur. Heart J., **37**(38), pp. 2858–2865.

[30] Packer, D. L., Kowal, R. C., Wheelan, K. R., Irwin, J. M., Champagne, J., Guerra, P. G., Dubuc, M., Reddy, V., Nelson, L., Holcomb, R. G., Lehmann, J. W., Ruskin, J. N., and STOP AF Cryoablation Investigators, 2013, "Cryoballoon Ablation of Pulmonary Veins for Paroxysmal Atrial Fibrillation: First Results of the North American Arctic Front (STOP AF) Pivotal Trial," J. Am. Coll. Cardiol., **61**(16), pp. 1713–1723.

[31] Lalonde, J.-P., Groves, R. E., Laske, T. G., Iaizzo, P. A., and Bischof, J. C., 2015, "Feedback System for Cryoablation of Cardiac Tissue," Patent No. US20150119868A1.

[32] Cahill, D. G., and Pohl, R. O., 1987, "Thermal Conductivity of Amorphous Solids Above the Plateau," Phys. Rev. B, **35**(8), pp. 4067–4073.

[33] Hodges, W., and Dames, C., 2019, "A Multi-Frequency 3ω Method for Tracking Moving Phase Boundaries," Rev. Sci. Instrum., **90**(9), p. 094903.

[34] Zhang, Y., Wu, C., and Borca-Tasciuc, T., 2020, "Theoretical Modeling of a Thermal Wave Technique to Determine the Extent of the Freezing Region Surrounding a Cryoprobe," J. Appl. Phys., **127**(18), p. 185101.

[35] Lubner, S. D., Choi, J., Wehmeyer, G., Waag, B., Mishra, V., Natesan, H., Bischof, J. C., and Dames, C., 2015, "Reusable bi-Directional 3ω Sensor to Measure Thermal Conductivity of 100-μm Thick Biological Tissues," Rev. Sci. Instrum., **86**(1), p. 014905.

[36] Natesan, H., Hodges, W., Choi, J., Lubner, S., Dames, C., and Bischof, J., 2016, "A Micro-Thermal Sensor for Focal Therapy Applications," Sci. Rep., **6**(1), p. 21395.

[37] Tian, L., Li, Y., Webb, R. C., Krishnan, S., Bian, Z., Song, J., Ning, X., Crawford, K., Kurniawan, J., Bonifas, A., Ma, J., Liu, Y., Xie, X., Chen, J., Liu, Y., Shi, Z., Wu, T., Ning, R., Li, D., Sinha, S., Cahill, D. G., Huang, Y., and Rogers, J. A., 2017, "Flexible and Stretchable 3ω Sensors for Thermal Characterization of Human Skin," Adv. Funct. Mater., **27**(26), p. 1701282.

[38] Webb, R. C., Pielak, R. M., Bastien, P., Ayers, J., Niittynen, J., Kurniawan, J., Manco, M., Lin, A., Cho, N. H., Malyrchuk, V., Balooch, G., and Rogers, J. A., 2015, "Thermal Transport Characteristics of Human Skin Measured In Vivo Using Ultrathin Conformal Arrays of Thermal Sensors and Actuators," PLoS One, **10**(2), p. e0118131.

[39] Lee, S. P., Klinker, L. E., Ptaszek, L., Work, J., Liu, C., Quivara, F., Webb, C., Dagdeviren, C., Wright, J. A., Ruskin, J. N., Slepian, M., Huang, Y., Mansour, M., Rogers, J. A., and Ghaffari, R., 2015, "Catheter-Based Systems With Integrated Stretchable Sensors and Conductors in Cardiac Electrophysiology," Proc. IEEE, **103**(4), pp. 682–689.

[40] Klinker, L., Lee, S., Work, J., Wright, J., Ma, Y., Ptaszek, L., Webb, R. C., Liu, C., Sheth, N., Mansour, M., Rogers, J. A., Huang, Y., Chen, H., and Ghaffari, R., 2015, "Balloon Catheters With Integrated Stretchable Electronics for Electrical Stimulation, Ablation and Blood Flow Monitoring," Extreme Mech. Lett., **3**, pp. 45–54.

[41] Webb, R. C., Bonifas, A. P., Behnaz, A., Zhang, Y., Yu, K. J., Cheng, H., Shi, M., Bian, Z., Liu, Z., Kim, Y.-S., Yeo, W.-H., Park, J. S., Song, J., Li, Y., Huang, Y., Gorbach, A. M., and Rogers, J. A., 2013, "Ultrathin Conformal Devices for Precise and Continuous Thermal Characterization of Human Skin," Nat. Mater., **12**(11), pp. 938–944.

[42] Kim, D.-H., Lu, N., Ghaffari, R., Kim, Y.-S., Lee, S. P., Xu, L., Wu, J., Kim, R.-H., Song, J., Liu, Z., Viventi, J., de Graff, B., Elolampi, B., Mansour, M., Slepian, M. J., Hwang, S., Moss, J. D., Won, S.-M., Huang, Y., Litt, B., and Rogers, J. A., 2011, "Materials for Multifunctional Balloon Catheters With Capabilities in Cardiac Electrophysiological Mapping and Ablation Therapy," Nat. Mater., **10**(4), pp. 316–323.

[43] Dames, C., 2013, "Measuring the Thermal Conductivity of Thin Films: 3 Omega and Related Electrothermal Methods," Annu. Rev. Heat Transfer, **16**(1), pp. 7–49.

[44] Mishra, V., Hardin, C. L., Garay, J. E., and Dames, C., 2015, "A 3 Omega Method to Measure an Arbitrary Anisotropic Thermal Conductivity Tensor," Rev. Sci. Instrum., **86**(5), p. 054902.

[45] Cahill, D. G., Goodson, K., and Majumdar, A., 2002, "Thermometry and Thermal Transport in Micro/Nanoscale Solid-State Devices and Structures," ASME J. Heat Transfer, **124**(2), pp. 223–241.

[46] Dames, C., and Chen, G., 2005, "1ω,2ω, and 3ω Methods for Measurements of Thermal Properties," Rev. Sci. Instrum., **76**(12), p. 124902.

[47] Valvano, J. W., 2011, "Tissue Thermal Properties and Perfusion," *Optical-Thermal Response of Laser Irradiated Tissue*, A. J. Welch, M. J. C. van Gemert, eds., 2nd ed., Springer, Berlin, pp. 455–485.

[48] Incropera, F. P., 2011, *Fundamentals of Heat and Mass Transfer*, Wiley, Hoboken, NJ, p. 2249.

[49] Vargaftik, N. B., 1993, *Handbook of Thermal Conductivity of Liquids and Gases*, CRC Press, Boca Raton, FL, p. 362.

[50] Kim, Y.-H., Marom, E. M., Herndon, J. E., and McAdams, H. P., 2005, "Pulmonary Vein Diameter, Cross-Sectional Area, and Shape: CT Analysis," Radiology, **235**(1), pp. 43–49; discussion 49–50.

[51] Davalos, R., and Rubinsky, B., 2011, "Tissue Ablation With Irreversible Electroporation," Patent No. US8048067 B2.

[52] Sugrue, A., Maor, E., Ivorra, A., Vaidya, V., Witt, C., Kapa, S., and Asirvatham, S., 2018, "Irreversible Electroporation for the Treatment of Cardiac Arrhythmias," Expert Rev. Cardiovasc. Ther., **16**(5), pp. 349–360.